This is a preprint, the final version is subject to change, of the American Mineralogist (MSA)
Cite as Authors (Year) Title. American Mineralogist, in press.
(DOI will not work until issue is live.) DOI: http://dx.doi.org/10.2138/am-2016-5474

The effects of shear deformation on planetesimal core segregation: Results from in-situ X-ray micro-tomography

REVISION 1

Kasey A. Todd[1], Heather C. Watson[2], Tony Yu[3], Yanbin Wang[3]

[1]Northern Illinois University, [2]Rensselaer Polytechnic Institute, [3]Center for Advanced Radiation Sources, the University of Chicago

Abstract Keywords: Core formation; Microtomography; Permeability; Lattice Boltzmann

Abstract

It is well accepted that the Earth formed by the accretion and collision of small (10-100km), rocky bodies called planetesimals. W-Hf isotopic evidence from meteorites suggest that the cores of many planetesimals formed within a relatively short time frame of ~3 My. While a very hot, deep magma ocean is generally thought to have been the driving mechanism for core formation in large planetary bodies, it inadequately explains differentiation and core formation in small planetesimals due to temperatures potentially being insufficient for wide-scale silicate melting to occur. In order for these planetesimals to differentiate within such a relatively short time without a magma ocean, a critical melt volume of the metallic (core-forming) phase and sufficient melt connectivity and grain size must have existed in order to attain the required permeability and lead to efficient core formation. Shear deformation may increase the connectedness of melt and the permeability, and thus could have been a major contributing factor in the formation of planetesimal cores. This deformation may have been caused by large impacts and collisions experienced by the planetesimals in the early solar system. The purpose of this work is to test the hypothesis that shear deformation enhances the connectivity and permeability of Fe-S melt within a solid silicate (olivine) matrix, such that rapid core formation is plausible. A rotational Drickamer apparatus (RDA) was used to heat and torsionally deform a sample of solid olivine + FeS liquid through six steps of large-strain shear deformation. After each deformation step, X-ray microtomographs were collected in the RDA to obtain *in-situ* 3-dimensional images of the sample. The resulting digital volumes were processed and permeability simulations utilizing the lattice Boltzmann method were performed to determine the effect of shear deformation on connectivity and permeability within the sample. The resulting permeabilities of the sample at various steps of deformation are the same within uncertainty and do not exhibit a change with increasing deformation. Additionally, the migration velocity calculated from the permeability of the sample is not high enough for segregation to take place within the time frame of ~3 My. In addition to further constraining the mechanism of core formation in planetesimals, the image processing techniques developed in this study will be of great benefit to future studies utilizing similar methods.

This is a preprint, the final version is subject to change, of the American Mineralogist (MSA)
Cite as Authors (Year) Title. American Mineralogist, in press.
(DOI will not work until issue is live.) DOI: http://dx.doi.org/10.2138/am-2016-5474

Introduction

Core formation is a significant, yet not completely understood process in the formation of the terrestrial planets and other small, rocky bodies such as large asteroids and satellites. Hafnium-Tungsten isotopic studies of the Earth's mantle and several meteorites indicate that the Earth's core likely formed in ~30-100 My after the formation of the proto-earth, while the parent bodies of iron meteorites differentiated much faster (~1-5 My) (Kleine et al., 2002; Scherstén et al., 2006; Rubie et al., 2007; Burkhardt et al., 2008; Kleine et al., 2009), and perhaps even before 1 My (Kruijer et al. 2014). This short timescale of 1-5 My for core formation is in agreement with the theoretical model that accretion in the early solar system took place relatively rapidly (Alexander et al., 2001; Wood et al., 2006; Rubie et al., 2007). The mechanism by which core formation took place in planetesimals is largely dependent upon the thermal history of the body (Rubie et al., 2007). Heat generated from ^{26}Al decay would have melted the core forming alloy in planetesimals 10-100 km in diameter (Yoshino et al., 2003; Walter and Tronnes, 2004; Bizzarro et al., 2005), but may not have melted the silicate to a significant degree. In the absence of widespread silicate melting, the mechanism by which metal and silicate might have segregated in planetsimals is limited to inter-granular percolation of metallic melt through a solid silicate matrix (Yoshino et al., 2003; Watson and Roberts, 2011).

In order for core formation to take place efficiently in an equilibrium setting, the metallic melt must be fully connected within the solid silicate (e.g. Roberts et al., 2007; Watson and Roberts, 2011). Whether or not connectivity is achieved depends on the dihedral (wetting) angle between the liquid and solid grains (von Bargen and Waff, 1986). The dihedral angle (θ) can be

This is a preprint, the final version is subject to change, of the American Mineralogist (MSA)
Cite as Authors (Year) Title. American Mineralogist, in press.
(DOI will not work until issue is live.) DOI: http://dx.doi.org/10.2138/am-2016-5474

expressed as:

$$\frac{\gamma_{ss}}{2\gamma_{sl}} = \cos\left(\frac{\theta}{2}\right)$$

where γ_{ss} and γ_{sl} refer to the solid-solid and the solid-liquid interfacial energies, respectively (Bulau and Waff, 1979). A dihedral angle less than 60° leads to a fully interconnected melt network in which percolation is possible even at extremely small melt volumes; while a dihedral angle greater than 60° results in isolated pockets of melt and inefficient core formation, unless a critical volume of melt is present. This critical volume of melt is known as the connectivity threshold and increases with increasing dihedral angle (von Bargen and Waff, 1986).

Experiments performed at conditions relevant to the interiors of planetesimals (~1-3 GPa) have determined that for the sulfide/metal melt-solid silicate system the dihedral angle is greater than 60° (e.g. Ballhaus and Ellis, 1996; Shannon and Agee, 1996; Gaetani and Grove, 1999; Holzheid et al., 2000; Takafuji et al., 2004; Walte et al., 2007), with an average angle of 90°±5°. At a dihedral angle greater than 60°, the melt within planetesimals would only have percolated to the core until the pinch-off threshold was reached, below which the remaining melt would have become stranded in the solid silicate matrix (von Bargen and Waff, 1986). The pinch-off threshold, determined to be between 3 and 6 vol% (Yoshino et al., 2003; Roberts et al., 2007; Watson and Roberts, 2011), is slightly below the percolation threshold. Therefore, being able to quantify the critical volume of melt (percolation threshold) required in order to maintain percolative flow becomes essential in understanding the processes that contributed to rapid, efficient core formation in planetesimals (Watson and Roberts, 2011).

Estimates of the connectivity threshold in the olivine + FeS system range from ~4 to ~17%, (Yoshino et al., 2003; Terasaki et al., 2008; Bagdassarov et al., 2009a, 2009b; Watson

This is a preprint, the final version is subject to change, of the American Mineralogist (MSA)
Cite as Authors (Year) Title. American Mineralogist, in press.
(DOI will not work until issue is live.) DOI: http://dx.doi.org/10.2138/am-2016-5474

and Roberts, 2011) with most accepted values being around 5 vol%. Although we don't have many meteorite samples of differentiated mantle materials, it is commonly thought that it is unlikely for 5vol% of metal to remain in the mantle. If we assume that core formation efficiently removes most core material from the mantle, an alternative segregation mechanism is required in order to lead to efficient core formation. For conditions within planetesimals, deformation caused by large impacts, and possibly convection, has been suggested as a mechanism that may have aided in the enhanced permeability and thus the segregation of the remaining melt (Bruhn et al., 2000; Rushmer et al., 2005; Groebner and Kohlstedt, 2006; Hustoft and Kohlstedt, 2006). This manner of efficient core formation via deformation would preclude the necessity of widespread silicate melting (i.e. a magma ocean), particularly in smaller planetesimals that may have never reached high enough temperatures.

Experiments performed on samples of varying compositions and melt volumes indicate that shear deformation can lead to the enhanced segregation of metallic melt from a solid silicate matrix (Bruhn et al., 2000; Rushmer et al., 2005; Groebner and Kohlstedt, 2006; Hustoft and Kohlstedt, 2006). Deformation induced on these samples had varying outcomes, including: the enhanced interconnection of melt pockets at 4 and 7 vol% sulfide melt (Bruhn et al., 2000) the migration of melt within a solid silicate matrix (Rushmer et al., 2005; 20-25 vol%), the formation of a strong melt-preferred orientation of previously isolated melt pockets (Groebner and Kohlstedt, 2006; 4 vol%), and evidence of grain boundary percolation down to a pinch-off threshold of ~1 vol% (Hustoft and Kohlstedt, 2006; 3, 5, and 9 vol%). The results of these experiments support the idea that shear deformation may lead to the more efficient segregation of metallic melt from a solid silicate matrix at melt volumes close to and above 5 vol%. The main differences between this previous work and the present study are (1) Some previous studies

This is a preprint, the final version is subject to change, of the American Mineralogist (MSA)
Cite as Authors (Year) Title. American Mineralogist, in press.
(DOI will not work until issue is live.) DOI: http://dx.doi.org/10.2138/am-2016-5474

looked at melt volumes that were already significantly connected (i.e. Rushmer et al. 2005), (2) In some cases, the experiments were performed at lower pressure (300MPa) and strain rates up to 2 orders of magnitude higher than those here (e.g. Groebner and Kohstedt, 2006, Hustoft and Kohlstedt, 2006) and (3) The only other 3-D study (Bruhn et al. 2000) is on a relatively small volume (~35mm x 35mm x 25mm) that may not be fully representative of connectivity and permeability of the whole sample. Recent work by Walte et al. (2011) suggests that the behavior of metallic melt in similar systems (olivine + FeS or Au) is dominated by surface energy at low strain rates and actaully may inhibit elongation of melt particles, and that melt may become concentrated into larger melt pockets.

The objective of the present study is to observe the effect of shear deformation on the permeability of an olivine + FeS sample that is close to the pinch-off threshold of ~3-6 vol% melt. Previous studies have relied upon methods, such as electrical conductivity (e.g. Yoshino, 2003, 2004), and using theoretical models based on 2-D images of melt geometry (e.g. Hustoft and Kohlstedt, 2006) that indirectly measure permeability by constraining the connection threshold. Recently, synchrotron based X-ray micro-tomography (3D) analysis of quenched samples (Shi et al. 2013) and quenched samples coupled with numerical simulations on both the olivine-basalt system (Zhu et al. 2011, Miller et al. 2014) and the olivine Fe-S system (Watson and Roberts 2011, have demonstrated that X-ray tomography is a useful tool in determining the permeability and melt geometry in a more direct way than previous methods. 2-D X-ray radiography at high pressure and temperature has recently been employed to observe the segregation process in-situ (Gotou et al. 2015). Here, we combine the advantages of each of these techniques. By using *in-situ* high pressure X-ray micro-tomography (HP-XMT) coupled with numerical simulations to monitor the evolution of the same sample as it is undergoing

This is a preprint, the final version is subject to change, of the American Mineralogist (MSA)
Cite as Authors (Year) Title. American Mineralogist, in press.
(DOI will not work until issue is live.) DOI: http://dx.doi.org/10.2138/am-2016-5474

heating and deformation we evaluate the effect of deformation on the core segregation process.

Experimental Methods

Sample Synthesis and High Pressure X-ray Microtomography

Starting materials consisted of optically clear San Carlos olivine crystals ($[MgO_{0.91}Fe_{0.09}]_2SiO_4$) and troilite powder (FeS). After grinding under ethanol using an agate mortar and pestle, the olivine was sieved to a grain size of 37-74 micrometers. Pure, powdered FeS (Alfa Aesar) was added to the dried olivine to comprise 4.5 vol% and the mixture was mixed again under ethanol further to ensure uniformity. The olivine and FeS mixture was packed into a graphite capsule and sintered in a piston-cylinder apparatus at RPI for 20 hours at 1 GPa and 1250°C. The sample synthesis assembly is shown in Figure 1a. Previous work indicates that these conditions allow the sample to attain close to complete textural equilibrium (e.g. Gaetani and Grove, 1999; Yoshino et al., 2003; Roberts et al., 2007; Watson et al., 2010). Once retrieved, the sintered sample was shaped with a diamond file into several 1x1 mm cylinders and prepared for high-pressure deformation and imaging experiments. Filing also served to remove the thin coating of graphite around the edge of the sintered samples.

The quenched and equilibrated sample was brought to the Advanced Photon Source (APS) at Argonne National Laboratory for *in-situ* deformation and tomographic imaging at Sector 13 (GeoSoilEnviroCARS; GSECARS), Beamline 13-BM-D). The sample assembly used in the Drickamer cell at APS is shown in Figure 1(b). The details of the experimental set-up available for high pressure X-ray tomography microscopy (HPXTM) are described by Wang (2005) and Wang et al. (2011). Due to the large X-ray absorption contrast between the olivine and FeS metal, the two materials can be easily distinguished in the resulting tomographic images at a

154 photon energy of 37 keV (Wang et al., 2011). A major advantage of using HPXTM is that the
155 sample can be imaged *in-situ* at high pressure and temperature, and so the *evolution* of one
156 sample can be recorded and observed over time.

157 Tomographic image collection was performed using a 4-inch tube with a 5x objective
158 lens, resulting in a pixel size of 2 μm. The exposure time was 25 seconds per frame. White field
159 images were collected before and after each set of tomography images in order to remove
160 artifacts. The large Si (111) Bragg-Bragg monochromator allows easy switching between
161 monochromatic and white radiation in seconds (see Wang et al., 2011). Sample pressure was
162 monitored by energy-dispersive X-ray diffraction of the MgO pressure standard in the sample
163 assembly and was maintained at 10 tons (~1.5GPa ± 0.5GPa) during the experiment (Speziale et
164 al. 2001). Temperature was estimated through the use of a power curve calibrated at GSECARS
165 for this experimental assembly. Temperatures were 1100°C ± 100°C during the deformation
166 process and lowered to ~850°C during tomographic image collection. Shear strain was applied
167 to the sample by rotating the upper and lower tungsten carbide anvils at constant speed in
168 opposite directions, each at 90° steps (**Figure 2**), for a total of 180° of twist. Each step of
169 deformation lasted for approximately 1.25 hours. Using the total angular rotation (840°) and the
170 total duration of the experiment (6.25 hours), a maximum apparent shear strain rate of 7.70E-5 s^{-1}
171 was obtained. However, this is only a rough estimate of the strain rate experienced by the outer
172 diameter of the sample and is considered an upper bound due to slippage that occurs between the
173 rotating anvils and the sample during torsion. This strain rate is lower than that reported by
174 previous workers on a similar system (e.g. Groebner and Kohlstedt, 2006, Hustoft and Kohlstedt,
175 2006), where strain rates varied from 10^{-2} to 10^{-4}. Walte et al. 2011 report similar strain rates to
176 our reported maximum ($7x10^{-6} – 1x10^{-4}$).

This is a preprint, the final version is subject to change, of the American Mineralogist (MSA)
Cite as Authors (Year) Title. American Mineralogist, in press.
(DOI will not work until issue is live.) DOI: http://dx.doi.org/10.2138/am-2016-5474

177 **Electron Microprobe Analysis**

178 Backscattered electron (BSE) imaging, secondary electron (SE) imaging, and
179 wavelength-dispersive spectroscopy (WDS) were conducted on both an undeformed sample of
180 the starting material and the deformed sample using the Cameca SX100 electron microprobe at
181 Rensselaer Polytechnic Institute. All imaging was conducted at 15 kV, with a beam current of
182 50 nA. The BSE images in **Figure 3** show the basic textures for the undeformed and the
183 deformed samples. The textures of the two samples are clearly different, with FeS grains in the
184 deformed sample being much more stretched out and appear to have migrated along olivine grain
185 boundaries. The deformed texture can be seen in **Figure 3b**, where FeS is present along
186 individual olivine grain boundaries; while in the undeformed sample, FeS occupies triple-grain
187 junctions or grain corners as more equi-dimensional blobs (**Figure 3a**). The image of the
188 deformed sample was taken from the mid-area of the sample, neither at the edge or in the center,
189 and is broadly characteristic of the texture seen throughout the entire sample. The elongated
190 blobs are no necessarily co-directional with the direction of shear in the sample, and are not
191 uniformly aligned throughout the sample.

192 **Table 1** summarizes the electron microprobe composition measurements for sulfide and
193 olivine in both the undeformed and deformed samples. The FeS grains in the deformed sample
194 exhibit some quench texture (sulfide immiscibility); however, this internal structure appears to
195 have had only a slight effect on the resulting Fe and S measurements. The higher standard
196 deviations in measurements of the deformed sample could also be attributed to the sulfide grains
197 being thinner and more stretched out, making it more difficult to conduct measurements on a
198 single bleb due to the beam size of a few microns even in spot mode. We attribute the nickel
199 measured in the sulfide grains to an impurity in the FeS starting material. The small amount of

This is a preprint, the final version is subject to change, of the American Mineralogist (MSA)
Cite as Authors (Year) Title. American Mineralogist, in press.
(DOI will not work until issue is live.) DOI: http://dx.doi.org/10.2138/am-2016-5474

nickel present in the olivine both before and after the deformation experiment can be attributed to the fact that nickel is occasionally substituted for iron in the crystal lattice of olivine (Kohlstedt and Mackwell, 1987).

Results and Discussion

Image Analysis

Quantitative permeability measurements were acquired from the resulting HPXTM images. The individual radiographs collected from the beamline were reconstructed using the scientific data visualization program Tomo_Display (Rivers and Gualda, 2009; http://cars9.uchicago.edu/software/idl/tomography.html) and exported as a series of TIFF images. When these individual images are stacked they create a 3-dimensional volume of the sample. Six of these image stacks were chosen at increasing degrees of deformation (0°, 180°, 360°, 540°, 720°, and 840°; all at 10 tons of ram load) so that any change in permeability could be observed. Figure 4a shows a gray-scale XTM image of the sample after reconstruction. These gray-scale images were then binarized into regions of "melt" and "non-melt" using the program ImageJ (Rasband, 1997; Figure 4b). The appropriate threshold was determined by finding a value that would produce the correct proportion of "melt" regions given the expected value from both our synthetic starting material and initial BSE imaging of the starting material and post-deformation experiment. The melt volume percent was calculated for each image stack and found to be within one standard deviation of the starting material. The average melt fraction of the binarized XTM volumes in the X-direction is 4.36 ± 0.11% and an average of 4.44 ± 0.07% in the Z-direction, compared to the actual value of 4.5 vol%. The X- and Z-directions within the sample can be seen in **Figure 2**, and represent the two directions in which flow was simulated and

This is a preprint, the final version is subject to change, of the American Mineralogist (MSA)
Cite as Authors (Year) Title. American Mineralogist, in press.
(DOI will not work until issue is live.) DOI: http://dx.doi.org/10.2138/am-2016-5474

223 permeability calculated. These are the two bulk directions that we can measure given the 3-D
224 data. We performed calculations in both directions because of the potential to observe
225 anisotropy within the sample due to the shear strain applied to the sample, as well as due to
226 potential shortening of the sample as the experiment continued. Because the nature of rotational
227 shear results in a non-uniform strain distribution in the sample, this method we performed
228 calculations of several subvolumes from different areas of the sample at each degree of
229 deformation. There was no measurable difference in the resulting permeability in either direction,
230 however there was a well-defined anisotropy between the two direction (see Figure 6).
231 In order to approximate the true texture of the sample, the binarized XTM images were
232 compared to the higher resolution BSE images of the deformed sample. In **Figure 5**, the
233 binarized deformed sample is compared to a binarized XTM image, illustrating the similarities in
234 texture and melt distribution between the two images. After the binarization process, the six
235 image stacks, all with dimensions of 450x450x150 pixels, were each divided into nine
236 150x150x150 pixel sub-volumes and converted into digital volume input files in MATLAB®.
237
238 **Lattice Boltzmann Simulations**
239 The lattice-Boltzmann method applied to 3-D digital rock samples has been shown to be
240 a fast and accurate method of quantifying permeability of complex geometries found in natural
241 porous systems (e.g. White et al. 2006). Here, quantitative permeability calculations were
242 performed on the digital volumes using the open-source program Palabos (Latt, 2009), which
243 utilizes the lattice Boltzmann method (LBM) to simulate flow of a viscous fluid through a matrix
244 while representing the physics of a real system (Chen and Doolen, 1998; Latt, 2008). Palabos
245 and the LBM have been used and validated by several previous studies (e.g. Bosl et al., 1998;

This is a preprint, the final version is subject to change, of the American Mineralogist (MSA)
Cite as Authors (Year) Title. American Mineralogist, in press.
(DOI will not work until issue is live.) DOI: http://dx.doi.org/10.2138/am-2016-5474

Roberts et al., 2007; Degruyter et al., 2010). Palabos uses Darcy's law to obtain the permeability of the sub-volumes in non-dimensional lattice units from the average velocity distribution throughout the 3-D volume, along with an applied pressure gradient and fluid viscosity. This non-dimensional value is then converted into physical units (m^2) by multiplying it with the pixel size of the XTM image.

The calculated permeabilities for various steps of shear strain for sample R1288 can be found in **Table 2**. The final measurements are all within one standard deviation of one another and do not increase with increasing deformation. Figure 6 plots the permeability results from two experiments against the steps of shear strain. The experiment labeled R1288 is the experiment shown in the images in this paper. The experiment labeled R1350 is a second experiment that was repeated using identical methods. The second experiment (R1350) was deformed to a significantly higher degree, although the final textures appeared to be similar. Also, the calculated permeabilities on both samples are consistent within uncertainty, and both sample show the sample anisotropy between the X and Z directions. This anisotropy may be a result of initial shortening of the sample due to compression at the initiation of the experiment. The one point at the highest degree of deformation in R1350 may indicate a slight shift upwards in permeability at very high degrees of deformation, but more work and experiments will need to be done to confirm this result. The quantitative analysis performed on the digital volumes allows for a more direct means to calculate the permeability of the sample than previous work that relied on models such as the Kozeny-Carman relationship relating permeability to grain size and model dependant geometric factors. The permeabilities obtained in this study are comparable to the range of values from previous workers' studies, particularly those of Roberts et al. (2007) and Watson and Roberts (2011). These studies both describe the olivine/sulfide system as well as

This is a preprint, the final version is subject to change, of the American Mineralogist (MSA)
Cite as Authors (Year) Title. American Mineralogist, in press.
(DOI will not work until issue is live.) DOI: http://dx.doi.org/10.2138/am-2016-5474

utilize XTM images to quantitatively determine permeability via lattice Boltzmann simulations. **Figure 7** compares these three studies to one another, where it can be seen that the permeabilities in this study are within one standard deviation of the permeabilities obtained for samples with higher melt fractions. It can also be seen that the results in this study have higher permeabilities than those of Watson and Roberts for the same melt fraction and the pre-deformation measurements are consistent with previous studies which state that the pinch-off threshold in the FeS-silicate system is between 3 and 6 vol% (Yoshino et al., 2003; Roberts et al., 2007; Watson and Roberts, 2011).

Comparison to Previous Studies

Several previous studies address the question of permeability and connectivity in similar samples with and without the complicating factor of deformation. The present work differs from these previous studies in a few important ways, as described below. In some previous work, the presence of an electrically conductive pathway has been interpreted as evidence for a melt that was sufficiently connected to allow for permeable flow (i.e. Yoshino et al., 2003, 2004). However, it has recently been shown (e.g. Watson and Roberts 2011, Watson et al. 2010) that small, disconnected, blebs of sulfide can create electrically conductive pathways. This is thought to be due to very thin (~nm) films along grain boundaries and edges even when the melt fraction is well below the percolation threshold (~1 vol% as opposed to 5 vol%). Because the difference in electrical conductivity is so drastic between the silicate and the sulfide melt, even a miniscule volume that is connected will produce significantly higher bulk conductivity. In these cases, the connected volume is such a small percentage of the total melt in the sample that it is unlikely to add any substantial permeability to the system. A more thorough discussion comparing estimates of permeability from electrical conductivity and x-ray micro-tomography measurements is

This is a preprint, the final version is subject to change, of the American Mineralogist (MSA)
Cite as Authors (Year) Title. American Mineralogist, in press.
(DOI will not work until issue is live.) DOI: http://dx.doi.org/10.2138/am-2016-5474

available in Watson and Roberts, (2011).

There have also been previous studies of the effect of deformation on connectivity and permeability in olivine + iron sulfide systems (e.g. Bruhn et al. 2000, Groebner and Kohlstedt, 2006, Hustoft et al. 2007, and Walte et al. 2011). Bruhn et al. (2000) performed experiments with a comparable volume fraction of Fe-S melt in an olivine matrix and deformed the samples at a higher strain rate of between $10^{-4}s^{-1}$ and $10^{-3}s^{-1}$ at 1250°C and 300MPa. In backscattered electron images they observed similar (but more pronounced) changes in the shape of the Fe-S melt blobs. The pockets became larger, more elongated, and were aligned at an angle of ~20° with the shear plane. Bruhn et al. performed a 3-D reconstruction on a small portion of their sample (~35mm x 35mm x 25mm) by serial sectioning, and repeated BSE imaging. They interpret the changes in the melt pocket texture as evidence that melt can become interconnected and thus allow permeable flow even in systems with high dihedral angles, as a result of shear deformation. The benefit of this technique is enhanced spatial resolution of the shape of the Fe-S blob, but that comes at a cost of not being able to image as much of the sample (thousands to millions of grains and pockets), and therefore, perhaps not being able to assess the change in connectivity across the whole sample. Groebner and Kohlstedt (2006) expanded on the earlier work with more experiments on an analog system with an even higher dihedral angle of ~150° (olivine +4% Au). Again, they found a change in texture associated with deformation of the samples, and that the molten gold formed well connected melt bands at an angle of ~15° to the shear plane. They took these results as evidence that deformation may induce more efficient percolative flow with non-wetting melts than previously believed. Again, the strain rates of these experiments were at least 2-3 orders of magnitude higher than the maximum strain rate measured here. The theory behind these results and similar results relating to the effect of shear on silicate melt extraction in the

This is a preprint, the final version is subject to change, of the American Mineralogist (MSA)
Cite as Authors (Year) Title. American Mineralogist, in press.
(DOI will not work until issue is live.) DOI: http://dx.doi.org/10.2138/am-2016-5474

315 Earth is summarized in Kohlstedt and Holtzmann (2009).

316 Walte et al. (2011) performed a series of similar experiments on olivine + FeS, and
317 Olivine +Au across a broader range of strain rates (~10^{-4} s^{-1} - 10^{-6} s^{-1}). They analyzed the
318 resulting textures in 2-D sections of the samples, and found that the changes in textures could be
319 categorized into different types depending on the strain rate. They show that at high strain rates
320 (the stress dominated regime, above ~$10^{-4}s^{-1}$) the samples show linear zones of elongated melt
321 pockets, and that the degree of elongation increases with increased strain rate. At lower strain
322 rates (the surface tension dominated regime, below ~$10^{-5}s^{-1}$), liquid pockets are not linearly
323 aligned or significantly elongated. The textures seen in our experiments are consistent with an
324 intermediate texture between what was observed for the high and low strain rate samples. This is
325 also consistent with our measured maximum strain rate of $7.7x10^{-5}$ s^{-1}. Walte's et al. (2011)
326 experiments show that only a very small amount of melt is lost during the low strain rate
327 experiments, indicating that there is limited connectivity of the melt within the sample. All of the
328 experiments by Walte et al. (2011) show that at best, the melt segregation is inefficient, and at
329 least a 2-3vol% of the metallic melt is left behind in the sample, which is consistent with our
330 present results.

331 **Implications**

332 The permeabilities obtained in this study can be used to calculate the migration velocity
333 of a sulfide melt through an olivine matrix in order to determine if shear deformation can lead to
334 core formation in small (100 km) planetesimals within the 1-5 My time frame. The rate of
335 migration can be calculated using the relationship:

336 $$v = k\Delta\rho g/\eta$$

337 where k is the permeability, $\Delta\rho$ is the density difference between sulfide and olivine (2.0E+03

This is a preprint, the final version is subject to change, of the American Mineralogist (MSA)
Cite as Authors (Year) Title. American Mineralogist, in press.
(DOI will not work until issue is live.) DOI: http://dx.doi.org/10.2138/am-2016-5474

338 kg/m^3), g is the gravitational acceleration (0.1 m/s^2), and η is sulfide melt viscosity (0.01 kg/m·s),
339 after Roberts et al. 2007 and Watson et al. 2011. Using the average of the permeabilities (X-
340 direction; 6.31E-15 m^2), the migration velocity is calculated to be 0.4 cm/year. A migration
341 velocity of ~3.3 cm/year is necessary in order to fully segregate a metallic melt into the core of a
342 small planetesimal within 3 My (Watson and Roberts, 2011).

343 However, migration velocity is highly dependent on grain size. Figure 8 shows that for a
344 melt volume of 4.5%, and the conditions above, a grain size of approximately 230 μm is needed
345 in order to reach a migration velocity of 3.3 cm/year. These grain sizes are reasonable for small
346 planetesimals (Watson and Roberts, 2011). To obtain the migration velocities in Figure 6, the
347 Kozeny-Carman relationship was used to calculate the permeabilities at increasing grain sizes:

348 $$k = (1/C) \cdot d^2 \varphi^n$$

349 with C = 2000 (geometric constant), φ = 4.5 vol% (porosity), and n =2, with n being a scaling
350 exponent representing how close to the percolation threshold a system is. The actual grain sizes
351 in this study were between 40 and 80 μm, and so these small sizes could be a contributing factor
352 in the low permeabilities, and thus low migration velocities, observed in this sample. As
353 mentioned above, caution needs to be applied when we are using the Kozeny-Carman
354 relationship, as it is not uniquely determined for this system. The geometric terms chosen are
355 roughly similar to those that have been used with some success to describe the olivine/basalt
356 system at equilibrium, but it is unclear that these terms will apply equally well here. The main
357 purpose of this calculation is to illustrate that the permeabilities measured in this olivine/FeS
358 system are low compared to what is required for rapid core formation in planetesimals. It should
359 be noted that increasing the exponent n from n=2 to n=3 (the value used for fully connected melt
360 well above the percolation threshold by Faul, 1997 and Bourbie and Zinszer, 1985) decreases the

This is a preprint, the final version is subject to change, of the American Mineralogist (MSA)
Cite as Authors (Year) Title. American Mineralogist, in press.
(DOI will not work until issue is live.) DOI: http://dx.doi.org/10.2138/am-2016-5474

361 permeability of the system even further. Furthermore, the migration velocity is also highly
362 dependent on viscosity. The values calculated here can essentially be considered an upper bound,
363 as they represent viscosities at the relatively high temperatures of 1300^{o}C, where some silicate
364 melting would be expected. The viscosity of FeS melt at these high temperatures and pressures
365 between 1 and 2 GPa is around 0.005 kg/m·s (Kono et al. 2015). But, LeBlanc and Secco (1996)
366 showed that the viscosity of $Fe_{73}S_{27}$ melts increases by nearly an order of magnitude as the
367 temperature is lowered to ~1100^{o}C (the conditions of these experiments, and reasonable
368 conditions for this model of percolative core formation in the absence of silicate melt). Studies
369 that obtain permeability indirectly through methods such as electrical conductivity yield
370 migration velocities that differ by several orders of magnitude from this study and others that use
371 HPXTM. From their electrical conductivity experiments, Yoshino et al. (2003) estimate a
372 migration velocity of ~1-100 m/year. This significantly higher value may be attributed to thin
373 layers of sulfide melt between olivine grains that were unable to be imaged via XTM due to the
374 *in-situ* nature of the experiment and thus the decreased resolution. However, overall, the
375 possible contribution that these narrow connections may have to the calculated permeability is
376 likely insignificant (Roberts et al., 2007; Watson and Roberts, 2011). Instead, this great
377 difference likely stems from the fact that a direct measurement of permeability was not possible
378 and so the Kozeny-Carman relationship was relied upon to infer permeability. In this study, the
379 permeability was directly measured, thus the migration velocity calculated likely represents a
380 more realistic scenario for core formation.

381 The main perceived drawback to the tomography method presented here is that the spatial
382 resolution of the imaging is not able to capture the smallest threads of melt that could potentially
383 be connected, and create high permeability pathways. Given our measured voxel size, we

This is a preprint, the final version is subject to change, of the American Mineralogist (MSA)
Cite as Authors (Year) Title. American Mineralogist, in press.
(DOI will not work until issue is live.) DOI: http://dx.doi.org/10.2138/am-2016-5474

384 estimate that we can reliably image a feature that about 2-4 micrometers in diameter, especially
385 considering the large contrast between the two phases in our tomographic reconstructions. First,
386 we note that the sulfide melt that is contributing to the permeability of the sample is a small
387 fraction of the total melt in the sample (ie. most of the melt is not connected). We can calculate
388 the expected permeability of the sample given different fractions of melt that is well connected
389 (Figure 9). Here the data symbols represent lattice Boltzmann simulations run on artificial (ideal)
390 volumes with a cylindrical tubules of varying diameters along grain edges of cubic grains (150
391 micrometer edge length). The solid gray curve is the analytical solution to Darcy's law for the
392 same geometry (Turcotte, 2002). Here we can see that our observed permeability ($\sim 10^{-15}$ m^2)
393 corresponds to tubules approximately 2-3 micrometers in diameter. This is admittedly close to
394 the expected resolution of what we could measure. However, in order to achieve an order of
395 magnitude higher permeability, tubules of approximately 5.5 micrometers in diameter are
396 predicted which we would expect to see clearly, but we do not. Secondly, we can compare 2-D
397 images of the sample at different spatial resolution. Figure 10 shows an example of the
398 differences we can expect to see in thresholding a 2-D backscattered electron image of the
399 deformed sample. The first panel shows the original image, the second shows that high
400 resolution image thresholded directly, the fourth shows the thresholding results of an image that
401 was artificially reduced in resolution to mimic the resolution that we would achieve by
402 tomography (~2 micrometers per pixel). In both cases the images were thresholded to result in
403 4.6 vol% melt. Although there are some noticeable differences, the main difference tends to be
404 around the perimeter of the larger melt blobs, which is unlikely to add significantly to the
405 permeability. The lower resolution image does miss a few stand-alone pixels that appear in the
406 higher resolution image, but again, these few pixels are unlikely to make a large difference in the

measured permeability.

The permeabilities obtained here from the X-ray microtomographic images via lattice Boltzmann simulations indicate that the migration velocity is probably not high enough for complete core formation to take place in planetesimals within the 1-5 My time frame. However, there is still much work that can be done in order to increase our understanding of the effects of certain parameters such as strain rate, temperature, and metal/silicate composition on the melt connectivity, permeability, and migration velocity. These new results indicate that permeabilities obtained via XTM and the LBM are reliable and accurate; further work utilizing these methods is promising and will bring us even closer to understanding the complex and significant event of core formation in planetesimals. The development of in-situ high pressure x-ray tomography techniques allows for novel experiments to be conducted, including those that monitor the evolution of a system undergoing deformation and reaction. These new techniques greatly enhance the array of tools to investigate dynamic processes at high temperatures and pressures in more detail and with more accuracy than previously available.

Acknowledgements: We would like to thank Jared Singer for assistance with the electron microprobe at RPI, and E. Bruce Watson for use of the RPI experimental facilities to synthesize the samples. We also thank Nico Walte and an anonymous reviewer for comments that improved this paper. This work was supported by NSF grant GEO-1322022.

References

Alexander, C. O. D., Boss, A. P., & Carlson, R. W. (2001). The early evolution of the inner solar system: A meteoritic perspective. *Science*, 293(5527), 64-68.

Bagdassarov, N., Solferino, G., Golabek, G. J., & Schmidt, M. W. (2009a). Centrifuge assisted percolation of Fe–S melts in partially molten peridotite: time constraints for planetary core formation. *Earth and Planetary Science Letters*, 288(1), 84-95.

Bagdassarov N., Golabek, G.J., Solferino, G., Schmidt, M.W. (2009b). Constraints on the Fe–S melt connectivity in mantle silicates from electrical impedance measurements. *Physics of the Earth and Planetary Interiors*, 177, 139-146.

Ballhaus, C., & Ellis, D. J. (1996). Mobility of core melts during Earth's accretion. *Earth and planetary science letters*, 143(1), 137-145.

Bizzarro, M., Baker, J. A., Haack, H., & Lundgaard, K. L. (2005). Rapid timescales for accretion and melting of differentiated planetesimals inferred from 26Al-26Mg chronometry. *The Astrophysical Journal Letters*, 632(1), L41.

Bosl, W. J., Dvorkin, J., & Nur, A. (1998). A study of porosity and permeability using a lattice Boltzmann simulation. *Geophysical Research Letters*, 25(9), 1475-1478.

Bourbie, T., Zinzner, B. (1985). Hydraulic and acoustic properties as a function of porosity in Fontainebleau sandstone. *Journal of Geophysical Research*, 90 (B3) 11,524-11532.

Bruhn, D., Groebner, N., & Kohlstedt, D. L. (2000). An interconnected network of core-forming melts produced by shear deformation. *Nature*, 403(6772), 883-886.

Bulau, J. R., H. S. Waff, and J. A. Tyburczy (1979), Mechanical and thermodynamic constraints on fluid distribution in partial melts, *Journal of Geophysical Research: Solid Earth* 84(B11), 6102–6108.

Burkhardt, C., Kleine, T., Bourdon, B., Palme, H., Zipfel, J., Friedrich, J. M., & Ebel, D. S. (2008). Hf–W mineral isochron for Ca, Al-rich inclusions: age of the solar system and the timing of core formation in planetesimals. *Geochimica et Cosmochimica Acta*, 72(24), 6177-6197.

Chen, S., & Doolen, G. D. (1998). Lattice Boltzmann method for fluid flows. *Annual review of fluid mechanics*, 30(1), 329-364.

Degruyter, W., Burgisser, A., Bachmann, O., & Malaspinas, O. (2010). Synchrotron X-ray microtomography and lattice Boltzmann simulations of gas flow through volcanic pumices. *Geosphere*, 6(5), 470-481.

Faul, U. H. (1997). Permeability of partially molten upper mantle rocks from experiments and percolation theory. *Journal of Geophysical Research*, 102:B5, 10,299-10,311.

Gaetani, G. A., & Grove, T. L. (1999). Wetting of mantle olivine by sulfide melt: implications for Re/Os ratios in mantle peridotite and late-stage core formation. *Earth and Planetary Science Letters*, 169(1), 147-163.

Gotou, H., Yagi, T., Iizuka, R., Suzuki, A. (2015) Application of X-ray radiography to study the segregation process of iron from silicate under high pressure and high temperature. High Pressure Research, 35(2), 130-138.

Groebner, N., & Kohlstedt, D. L. (2006). Deformation-induced metal melt networks in silicates: Implications for core–mantle interactions in planetary bodies. *Earth and Planetary Science Letters*, 245(3), 571-580.

Holzheid, A., Schmitz, M. D., & Grove, T. L. (2000). Textural equilibria of iron sulfide liquids in partly molten silicate aggregates and their relevance to core formation scenarios. *Journal of Geophysical Research,* 105(B6), 13555-13.

Hustoft, J. W., & Kohlstedt, D. L. (2006). Metal-silicate segregation in deforming dunitic rocks. *Geochemistry, Geophysics, Geosystems*, 7(2).

Kleine, T., Münker, C., Mezger, K., & Palme, H. (2002). Rapid accretion and early core formation on asteroids and the terrestrial planets from Hf–W chronometry. *Nature*, 418(6901), 952-955.

Kleine, T., Touboul, M., Bourdon, B., Nimmo, F., Mezger, K., Palme, H., & Halliday, A. N. (2009). Hf–W chronology of the accretion and early evolution of asteroids and terrestrial planets. *Geochimica et Cosmochimica Acta*, 73(17), 5150-5188.

Kohlstedt, D. L., & Mackwell, S. J. (1987). High-temperature stability of San Carlos olivine. *Contributions to Mineralogy and Petrology*, *95*(2), 226-230.

Kohlstedt , D.L., and Holtzmann, B.K. (2009). Shearing melt out of the earth: An experimentalist's perspective on the influence of deformation on melt extraction. *Annual Reviews in Earth and Planetary Science*. 37: 561-93.

Kono, Y., Kenney-Benson, C., Shibazaki, Y., Park, C., Shen, G., Wang, Y. (2015). High-pressure viscosity of liquid Fe and FeS revisited by falling sphere viscometry using ultrafast X-ray imaging. *Physics of the Earth and Planetary Interiors*. 241, 57-64.

Latt, J. (2008). Choice of units in lattice Boltzamnn Simulation. *Lattice Boltzmann Howtos: http://www.lbmethod. org/howtos: main.*

Latt, J. (2009). Palabos, Parallel Lattice Boltzmann Solver. *http://www.Palabos.com.*

LeBlanc, G.E., Secco, R.A. (1996) Viscosity of an Fe-S liquid up to 1300øC and 5 GPa. Geophysical Research Letters. 23(3) 213-216.

Miller, K.J., Zhu, W., Montesi, L.G.J., Gaetani, G. (2014) Experimental quantification of permeability of partially molten mantle rock. *Earth and Planetary Science Letters*. 388, 273-282.

Rivers, M.L., and Gualda, G.A.R., 2009, 'tomo_display' and 'vol_tools': IDL VM packages for tomography data reconstruction, processing, and visualization, Eos Transactions of AGU, Joint Assembly Supplement.

Roberts, J. J., Kinney, J. H., Siebert, J., & Ryerson, F. J. (2007). Fe-Ni-S melt permeability in olivine: Implications for planetary core formation. *Geophysical Research Letters*, 34(14).

Rubie, D. C., Nimmo, F., & Melosh, H. J. (2007). Formation of Earth's core. *Treatise on Geophysics*, 9, 51-90.

Rushmer, T., Petford, N., Humayun, M., & Campbell, A. J. (2005). Fe-liquid segregation in deforming planetesimals: Coupling core-forming compositions with transport phenomena. *Earth and Planetary Science Letters*, 239(3), 185-202.

Scherstén, A., Elliott, T., Hawkesworth, C., Russell, S., & Masarik, J. (2006). Hf–W evidence for rapid differentiation of iron meteorite parent bodies. *Earth and Planetary Science Letters*, 241(3), 530-542.

Shannon, M. C., & Agee, C. B. (1996). High pressure constraints on percolative core formation. *Geophysical Research Letters*, 23(20), 2717-2720.

Shi, C, Y., Zhang, L., Yang, W., Liu, Y., Wang, J., Meng, Y., Andrews, J.C., Mao, W.L. 2013. Formation of an interconnected network of iron melt at Earth's lower mantle conditions. *Nature Geoscience*, 6, 971-975.

Speziale, S., Zha, C., Duffy, T.S., Hemley, R.J., Mao, H.K. (2001). Quasi-hydrostatic compression of magnesium oxide to 52 GPa: Implications for the pressure-volume-temperature equation of state. *Journal of Geophysical Research, Solid Earth*. 106: B1, 515–528.

Takafuji, N., Hirose, K., Ono, S., Xu, F., Mitome, M., & Bando, Y. (2004). Segregation of core melts by permeable flow in the lower mantle. *Earth and Planetary Science Letters*, 224(3), 249-257.

Terasaki, H., Frost, D. J., Rubie, D. C., & Langenhorst, F. (2008). Percolative core formation in planetesimals. *Earth and Planetary Science Letters*, 273(1), 132-137.

Tucotte, D.L., Schubert, G.(2002) Geodynamics. Second ed. Cambridge University Press. New York, NY. USA.

von Bargen, N., & Waff, H. S. (1986). Permeabilities, interfacial areas and curvatures of partially molten systems: Results of numerical computations of equilibrium microstructures. *Journal of Geophysical Research: Solid Earth* (1978–2012), 91(B9), 9261-9276.

Walte, N. P., Becker, J. K., Bons, P. D., Rubie, D. C., & Frost, D. J. (2007). Liquid-distribution and attainment of textural equilibrium in a partially-molten crystalline system with a high-dihedral-angle liquid phase. *Earth and Planetary Science Letters*, 262(3), 517-532.

Walte, N.P., Rubie, D.C., Bons, P.D., Frost, D.J. (2011) Deformation of a crystalline aggregate with a small percentage of high-dihedral-angle liquid: Implications for core-mantle differentiation during planetary formation. *Earth and Planetary Science Letters.* 305. 124-134.

Walter, M. J., & Trønnes, R. G. (2004). Early earth differentiation. *Earth and Planetary Science Letters*, 225(3), 253-269.

Wang, Y., Uchida, T., Westferro, F., Rivers, M. L., Nishiyama, N., Gebhardt, J., ... & Sutton, S. R. (2005). High-pressure x-ray tomography microscope: Synchrotron computed microtomography at high pressure and temperature. *Review of scientific instruments*, 76(7), 073709-073709.

Wang, Y., Lesher, C., Fiquet, G., Rivers, M. L., Nishiyama, N., Siebert, J., ... & Guyot, F. (2011). In situ high-pressure and high-temperature X-ray microtomographic imaging during large deformation: A new technique for studying mechanical behavior of multiphase composites. *Geosphere*, 7(1), 40-53.

Watson, H.C. Roberts, J.J., Tyburczy, J.A. (2010) Effect of conductive impurities on electrical conductivity in polycrystalline olivine. *Geophysical Research Letters* 37(2) L02302, doi:10.1029/2009GL041566

Watson, H. C., & Roberts, J. J. (2011). Connectivity of core forming melts: Experimental constraints from electrical conductivity and X-ray tomography. *Physics of the Earth and Planetary Interiors*, 186(3), 172-182.

White, J.A., Borja, R. I., Fredrich, J. T. (2006). Calculating the effective permeability of sandstone with multi-scale lattice Boltzmann/finite element simulations. Acta Geotechnica, 1, 195-209.

Wood, B. J., Walter, M. J., & Wade, J. (2006). Accretion of the Earth and segregation of its core. *Nature*, 441(7095), 825-833.

Yoshino, T., Walter, M. J., & Katsura, T. (2003). Core formation in planetesimals triggered by permeable flow. *Nature*, 422(6928), 154-157.

Yoshino, T., Walter, M.J., Katsura, T. (2004). Connectivity of molten Fe alloy in peridotite based on in situ electrical conductivity measurements: implications for core formation in terrestrial planets. *Earth and Planetary Science Letters*. 222(2), 625-643.

Zhu, W. Hirth, G. (2003) A network model for permeability in partially molten rocks. *Earth and Planetary Science Letters*. 212, 407-416.

Zhu, W., Gaetani, G., Fusseis, F., Montesi, L.G.J., De Carlo, F. 2011. Microtomography of partially molten rocks: Three dimensional melt distribution in mantle peridotite. *Science.* 332, 88-91.

Figure Captions

Figure 1. (a) ¾ " piston cylinder cell assembly used to synthesize the olivine + FeS starting material in a graphite capsule. (b) the assembly used for deformation experiments in the Drickamer cell.

Figure 2: Schematic illustration of the sample with the two directions of flow that permeability measurements were obtained from. The X-direction of flow is parallel to the axis of rotation, while the Z-direction is perpendicular.

Figure 3. BSE images of an undeformed sample and the deformed sample. **(a)** An undeformed sample and **(b)** the deformed sample, both sectioned parallel to the axis of rotation. The image of the deformed sample is from a location in the midpart of the sample (neither at the edge or at the center).

Figure 4. XTM image before and after binarization. **(a)** A gray-scale XTM image slice and **(b)** the same slice binarized. Melt is represented as the white areas, while non-melt (i.e. silicate matrix) is represented by black.

Figure 5. A binarized XTM image compared to a binarized BSE image. **(a)** Binarized XTM image of the sample deformed to 360° and **(b)** a binarized BSE image of the fully deformed sample. The texture and melt distribution in both images are very similar, indicating that the binarization process is successful in reproducing the sample texture.

Figure 6: Permeability vs. degrees of deformation for two experiments. The images depicting texture in this paper are all from the first experiment (labeled R1288). The second experiment was performed in an analogous manner, but experienced significantly more deformation. The resulting final textures are very similar between both experiments, and the permeability results are consistent within uncertainty.

Figure 7. Plot of melt fraction vs. permeability comparing the results of this work to previous work. The closed circle is permeability in the X-direction for this work (4.5 vol% melt) and the open circle is for the Z-direction, with each point being an average of the full volumes in each respective direction of flow. One permeability result is shown from Roberts et al. (2007) and six results are shown from Watson and Roberts (2011). The average of the nine permeabilities is represented by the horizontal dashed lines and the gray area represents one standard deviation from this average. The sample from Roberts et al. is 10 vol%, and the results from Watson and Roberts are ~4, ~6, and ~10 vol%. The uncertainties on the data point from Roberts et al. were not available.

Figure 8. Migration velocity plotted as a function of grain size at a melt volume of 4.5%. The vertical gray dashed line represents the minimum grain size necessary (~230 μm) to attain the minimum migration velocity needed (3.3 cm/yr) in order for a small (100 km) planetesimal to fully differentiate within 3 My.

Figure 9: Permeability versus tubule diameter for an idealized geometry of cubic grains of different sizes with melt tubes along grain edges. Symbols represent results from lattice Boltzmann simulations run on idealized artificial volumes, and curves are calculations of the permeability from Darcy's law for this simplified geometry.

Figure 10: (a) BSE image of post-run sample (b) thresholded high resolution BSE image (c). Original BSE image again. (d) thresholding of the same image that has been artificially reduced in resolution to approximate the tomography results .

This is a preprint, the final version is subject to change, of the American Mineralogist (MSA)
Cite as Authors (Year) Title. American Mineralogist, in press.
(DOI will not work until issue is live.) DOI: http://dx.doi.org/10.2138/am-2016-5474

Tables

Table 1.

Electron Microprobe Results.

Olivine (wt%) - Deformed							
	SiO_2	**FeO**	**MgO**	**NiO**	**SO**	**Total**	**No. of Analyses**
Average	40.10±0.28	10.55±0.26	50.28±0.24	0.04±0.01	0.04±0.03	101.02±0.16	54
Sulfide (wt%) - Deformed							
	Fe	**S**	**Si**	**Mg**	**Ni**	**Total**	**No. of Analyses**
	62.31±1.45	32.01±3.73	0.43±0.42	0.59±0.79	2.70±2.36	98.04±0.87	20
Olivine (wt%) - Undeformed							
	SiO_2	**FeO**	**MgO**	**NiO**	**SO**	**Total**	**No. of Analyses**
Average	40.25±0.20	10.70±0.08	50.58±0.09	0.05±0.01	0.03±0.05	101.61±0.21	44
Sulfide (wt%) - Undeformed							
	Fe	**S**	**Si**	**Mg**	**Ni**	**Total**	**No. of Analyses**
	59.21±0.45	35.62±0.45	0.17±0.16	0.04±0.04	3.54±0.22	98.58±0.55	21

σ = one standard deviation

This is a preprint, the final version is subject to change, of the American Mineralogist (MSA)
Cite as Authors (Year) Title. American Mineralogist, in press.
(DOI will not work until issue is live.) DOI: http://dx.doi.org/10.2138/am-2016-5474

Table 2.

Final Permeability Results for the Sample R1288 in the X- and Z-Directions.

Angle	Melt Fraction	σMF	Log(k)	σlog(k)
X-Direction				
0	4.39	0.56	-14.04	0.05
180	4.53	0.89	-14.24	0.05
360	4.34	0.54	-14.21	0.04
540	4.37	0.48	-14.19	0.04
720	4.34	0.53	-14.24	0.08
840	4.20	0.61	-14.27	0.06
Z-Direction				
0	4.32	0.85	-14.52	0.08
180	4.52	1.03	-14.74	0.09
360	4.42	0.68	-14.68	0.05
540	4.45	1.00	-14.78	0.07
720	4.46	1.02	-14.83	0.05
840	4.44	0.80	-14.69	0.11

σ = one standard deviation.

This is a preprint, the final version is subject to change, of the American Mineralogist (MSA)
Cite as Authors (Year) Title. American Mineralogist, in press.
(DOI will not work until issue is live.) DOI: http://dx.doi.org/10.2138/am-2016-5474

Figures

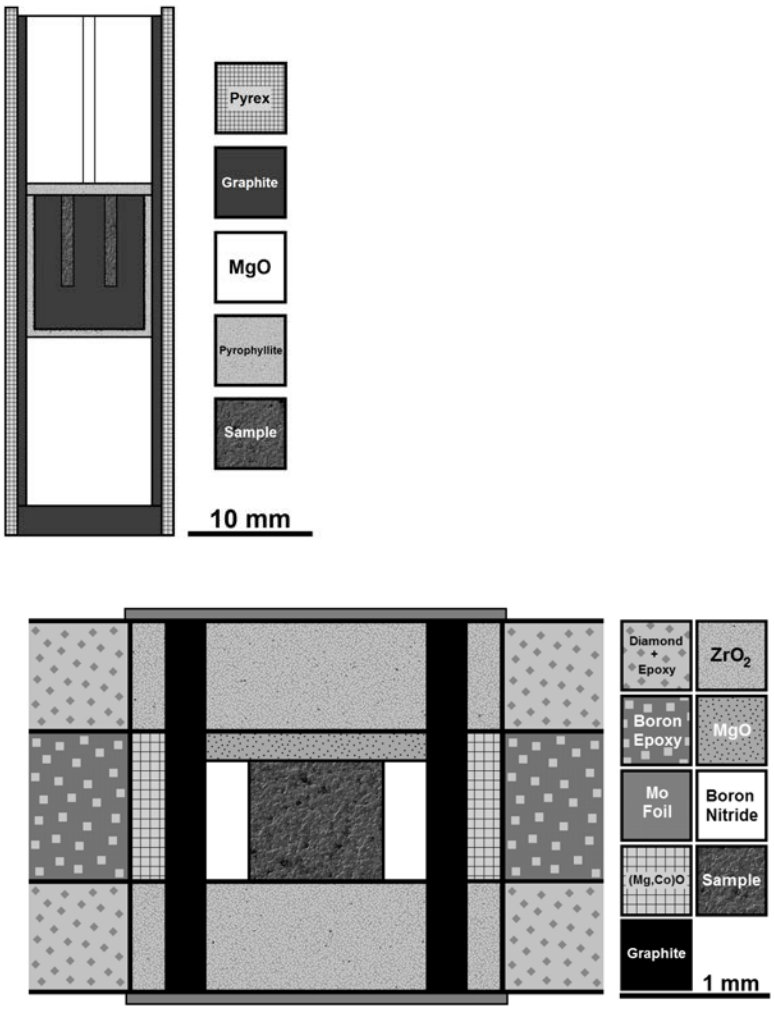

Figure 1.

This is a preprint, the final version is subject to change, of the American Mineralogist (MSA)
Cite as Authors (Year) Title. American Mineralogist, in press.
(DOI will not work until issue is live.) DOI: http://dx.doi.org/10.2138/am-2016-5474

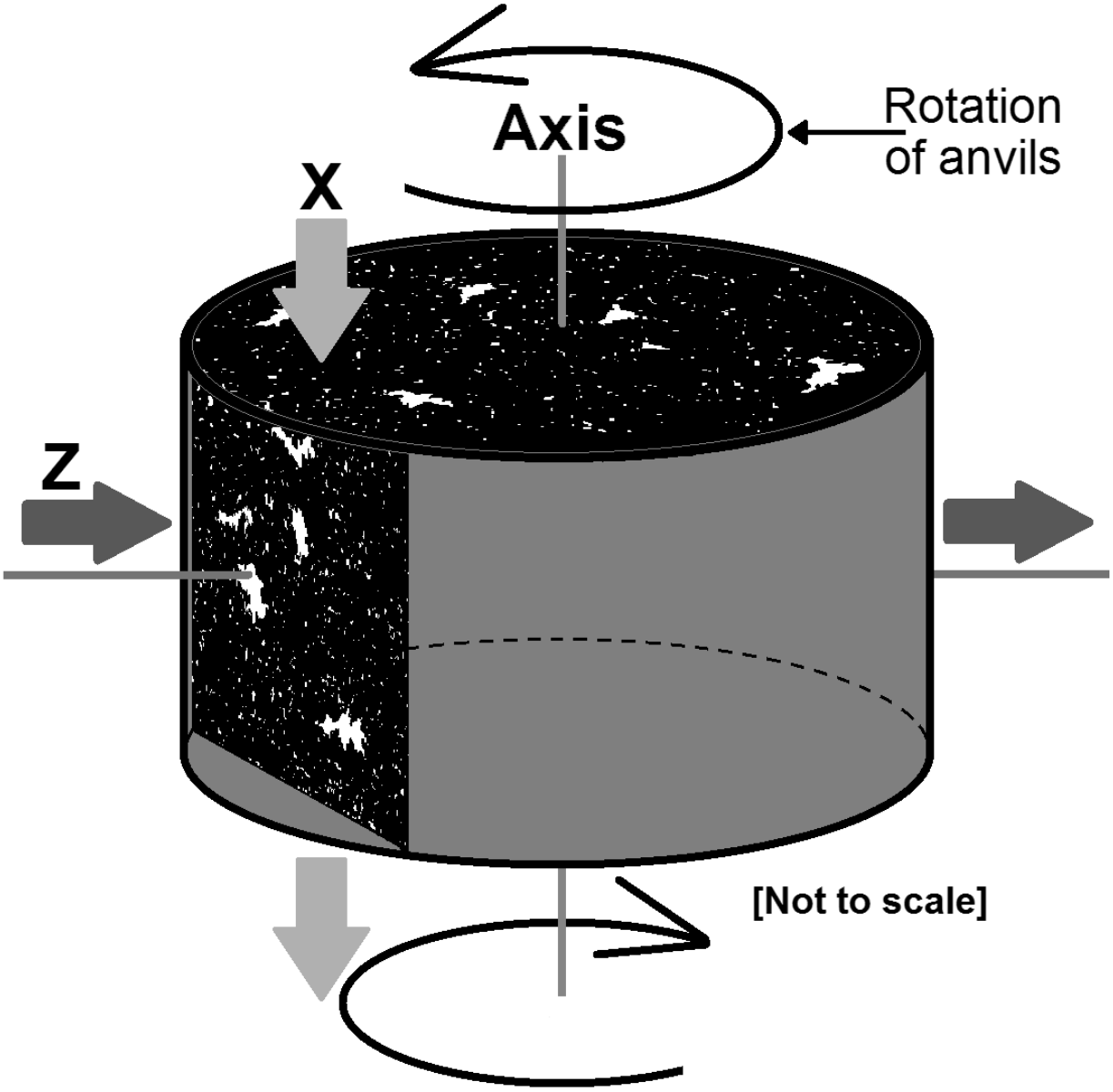

Figure 2.

This is a preprint, the final version is subject to change, of the American Mineralogist (MSA)
Cite as Authors (Year) Title. American Mineralogist, in press.
(DOI will not work until issue is live.) DOI: http://dx.doi.org/10.2138/am-2016-5474

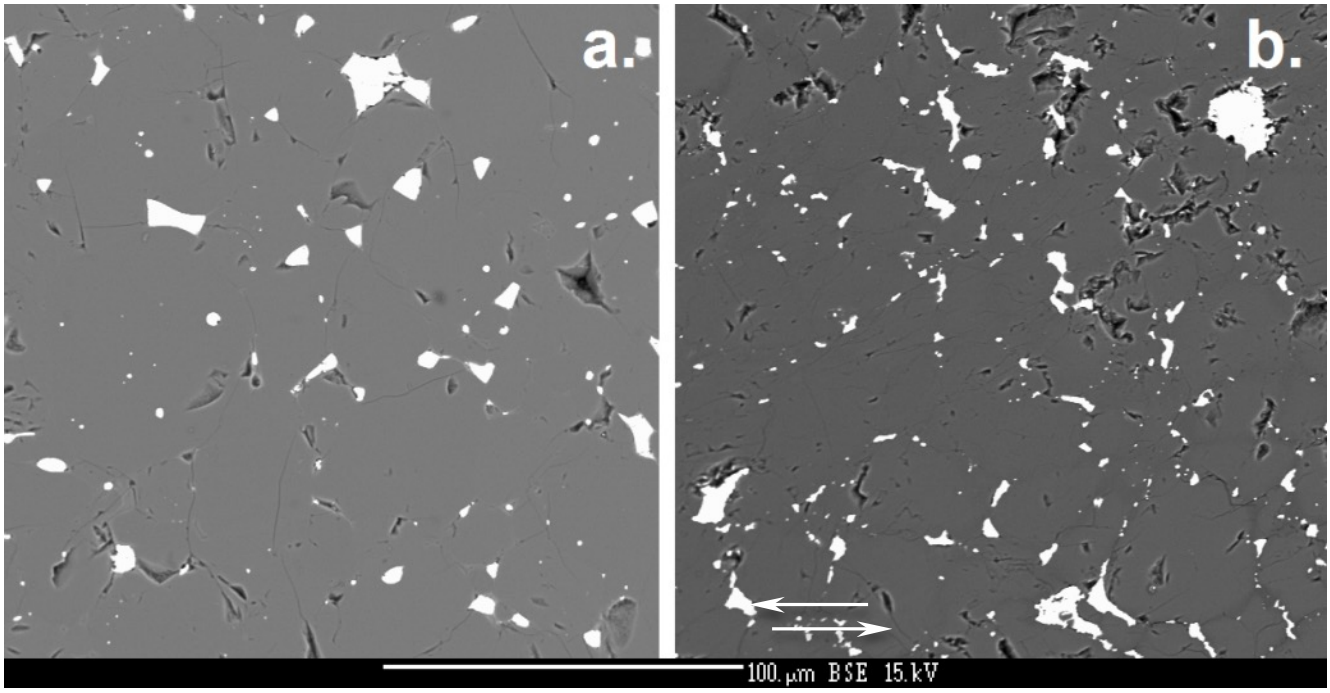

Figure 3.

This is a preprint, the final version is subject to change, of the American Mineralogist (MSA)
Cite as Authors (Year) Title. American Mineralogist, in press.
(DOI will not work until issue is live.) DOI: http://dx.doi.org/10.2138/am-2016-5474

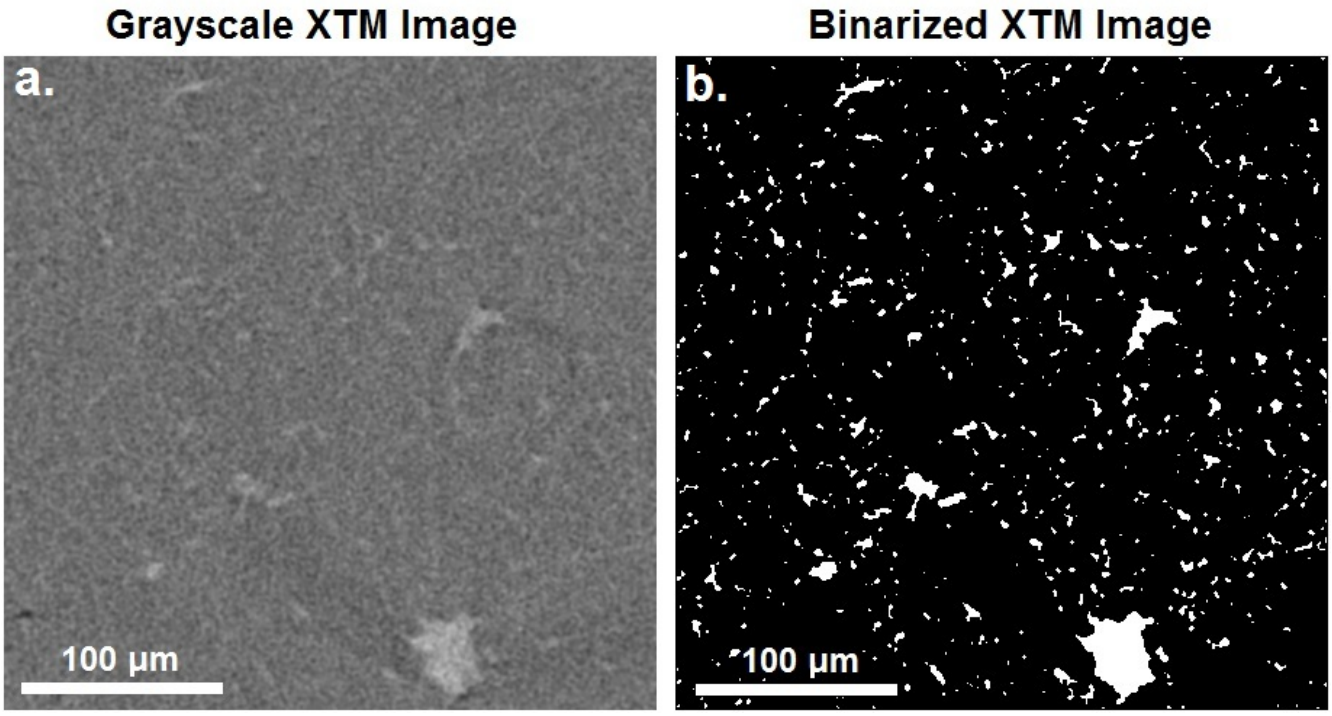

Figure 4.

This is a preprint, the final version is subject to change, of the American Mineralogist (MSA)
Cite as Authors (Year) Title. American Mineralogist, in press.
(DOI will not work until issue is live.) DOI: http://dx.doi.org/10.2138/am-2016-5474

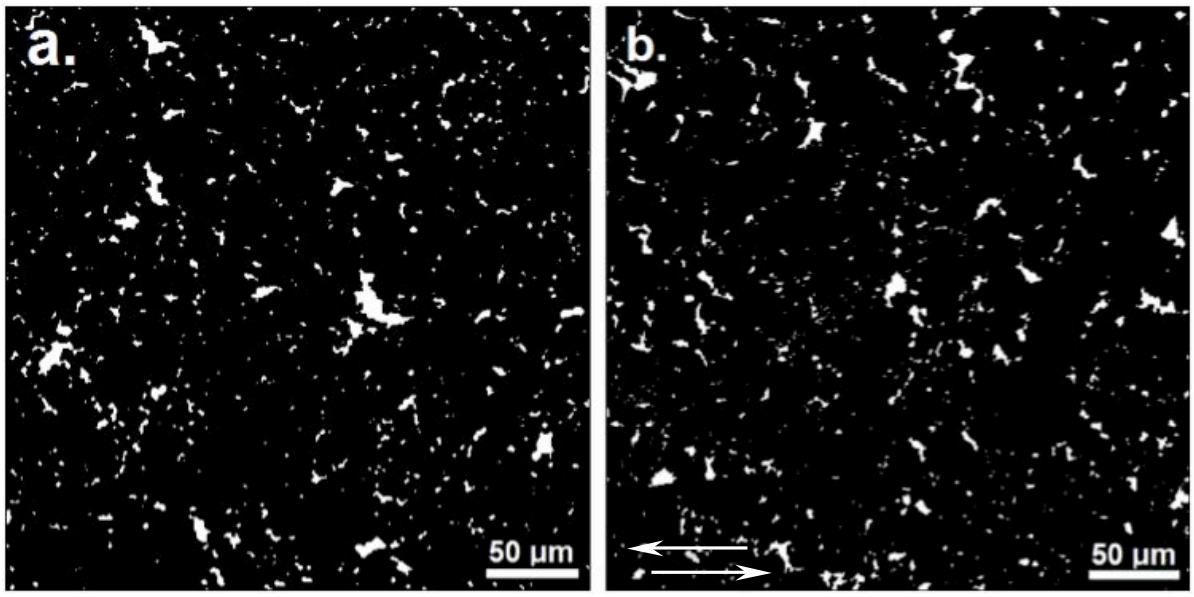

Figure 5.

This is a preprint, the final version is subject to change, of the American Mineralogist (MSA)
Cite as Authors (Year) Title. American Mineralogist, in press.
(DOI will not work until issue is live.) DOI: http://dx.doi.org/10.2138/am-2016-5474

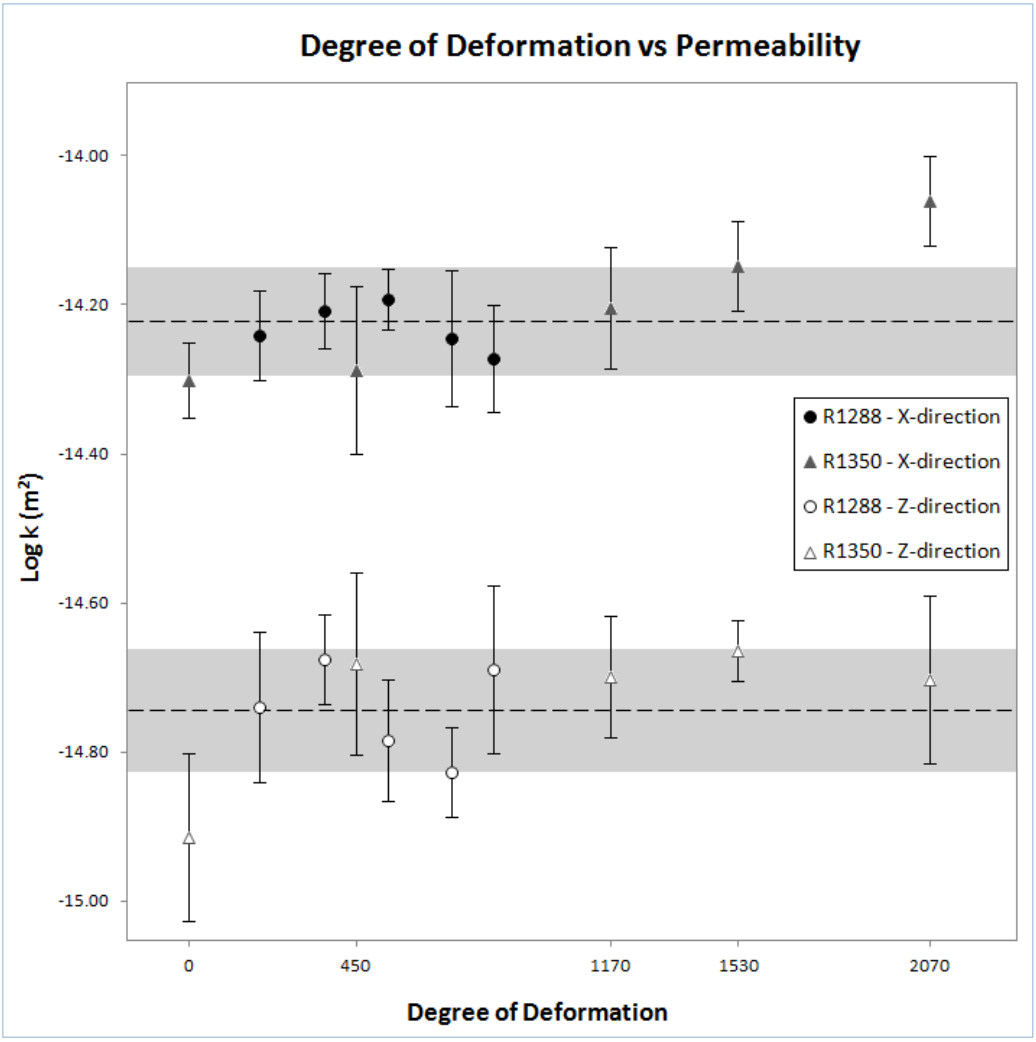

Figure 6

This is a preprint, the final version is subject to change, of the American Mineralogist (MSA)
Cite as Authors (Year) Title. American Mineralogist, in press.
(DOI will not work until issue is live.) DOI: http://dx.doi.org/10.2138/am-2016-5474

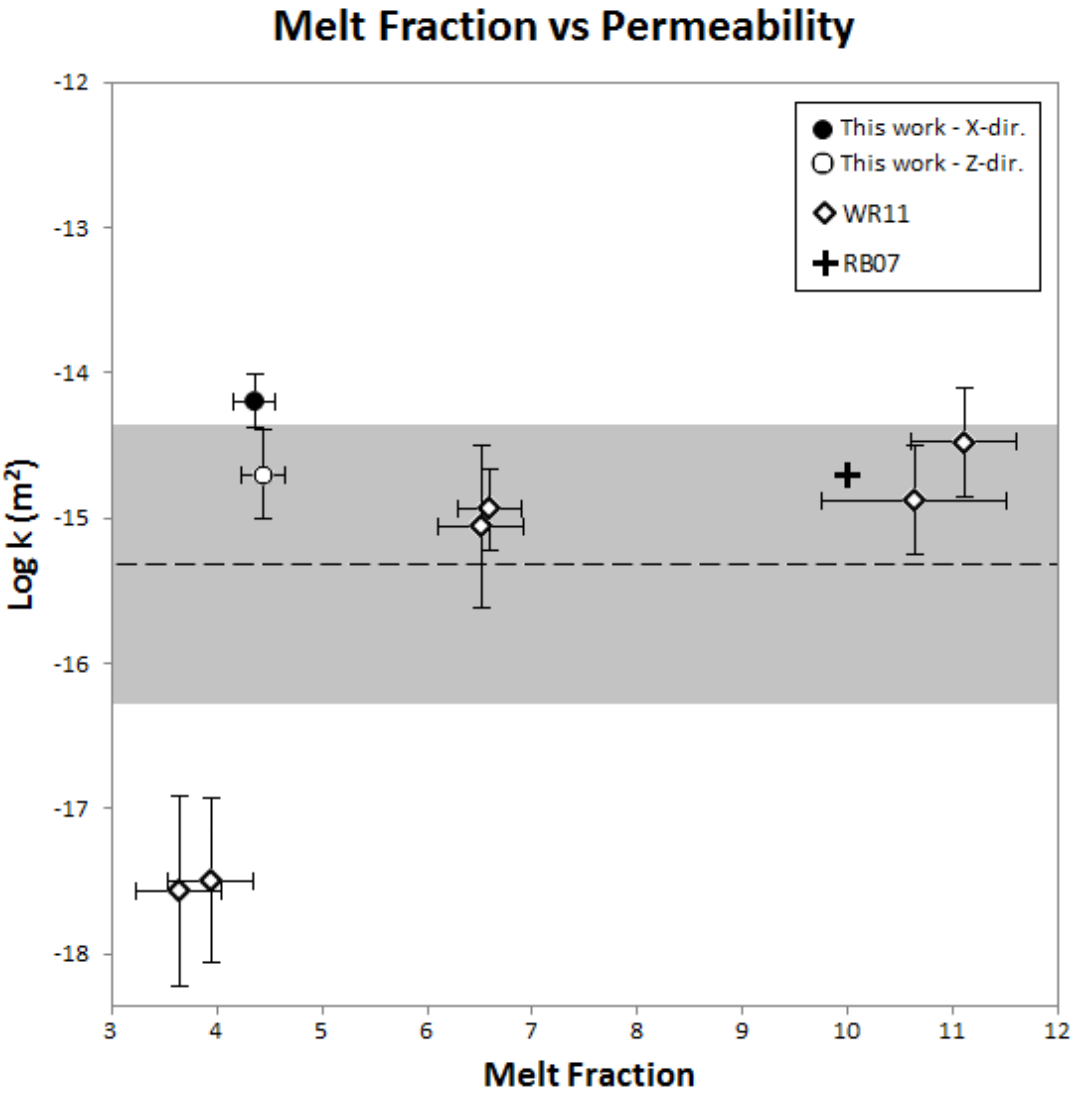

Figure 7.

This is a preprint, the final version is subject to change, of the American Mineralogist (MSA)
Cite as Authors (Year) Title. American Mineralogist, in press.
(DOI will not work until issue is live.) DOI: http://dx.doi.org/10.2138/am-2016-5474

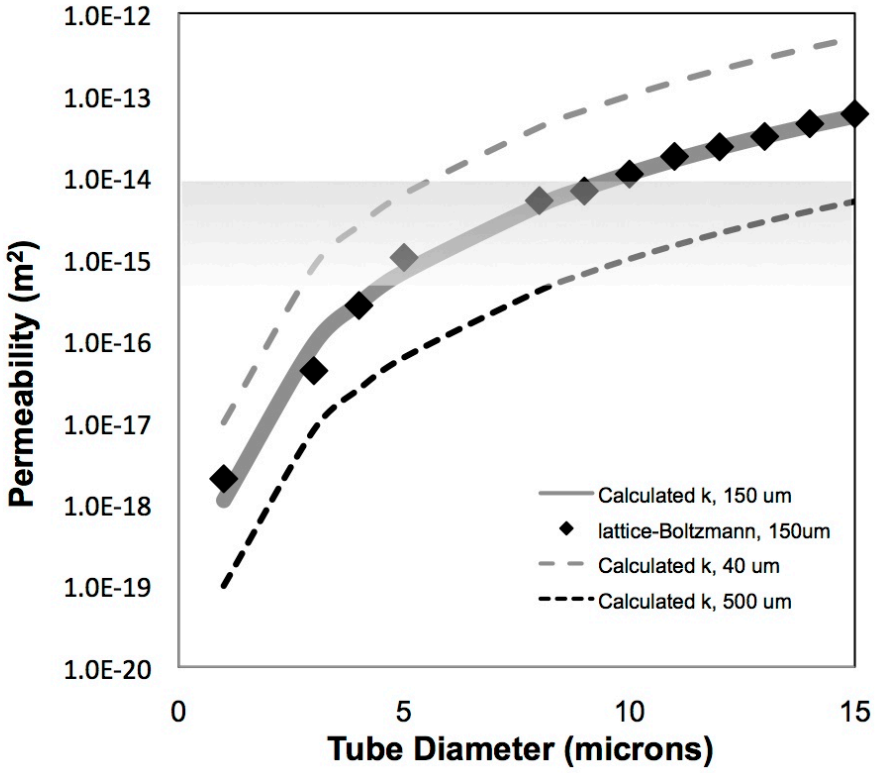

Figure 8.

This is a preprint, the final version is subject to change, of the American Mineralogist (MSA)
Cite as Authors (Year) Title. American Mineralogist, in press.
(DOI will not work until issue is live.) DOI: http://dx.doi.org/10.2138/am-2016-5474

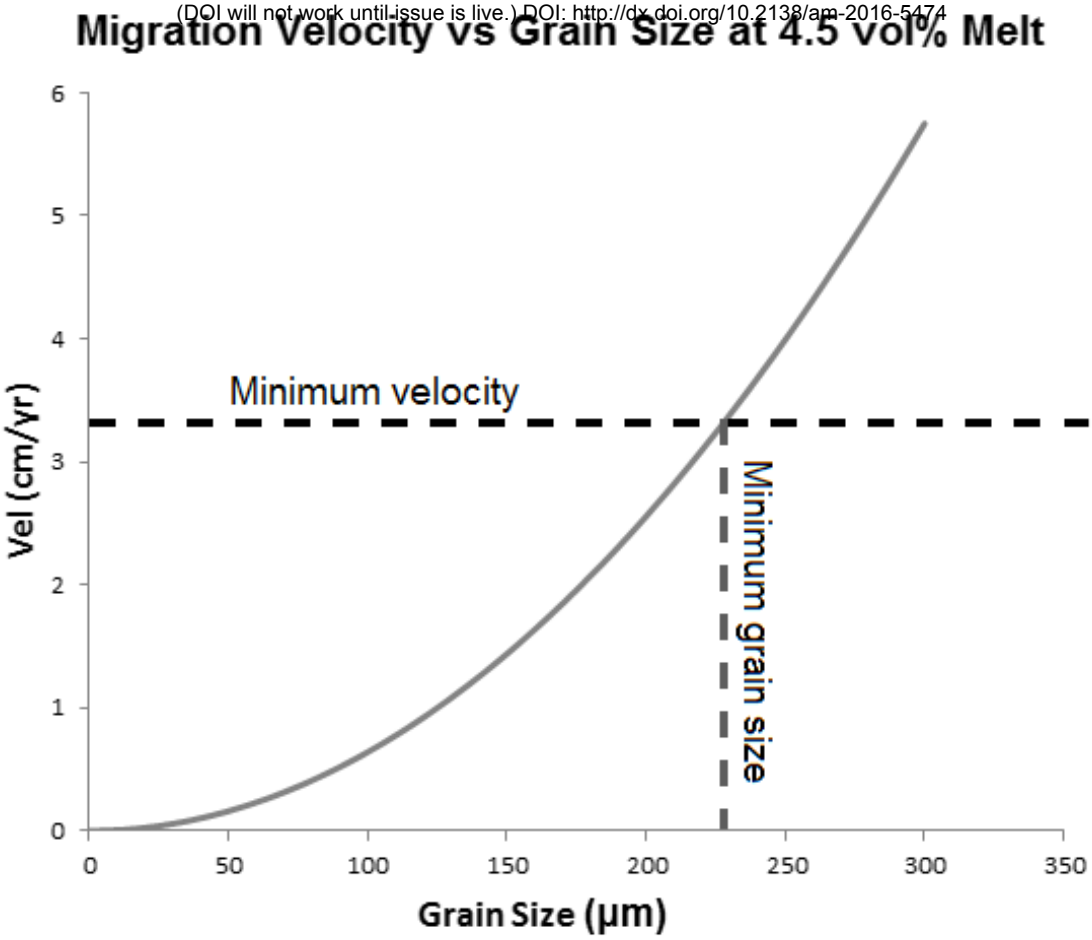

Figure 9

This is a preprint, the final version is subject to change, of the American Mineralogist (MSA)
Cite as Authors (Year) Title. American Mineralogist, in press.
(DOI will not work until issue is live.) DOI: http://dx.doi.org/10.2138/am-2016-5474

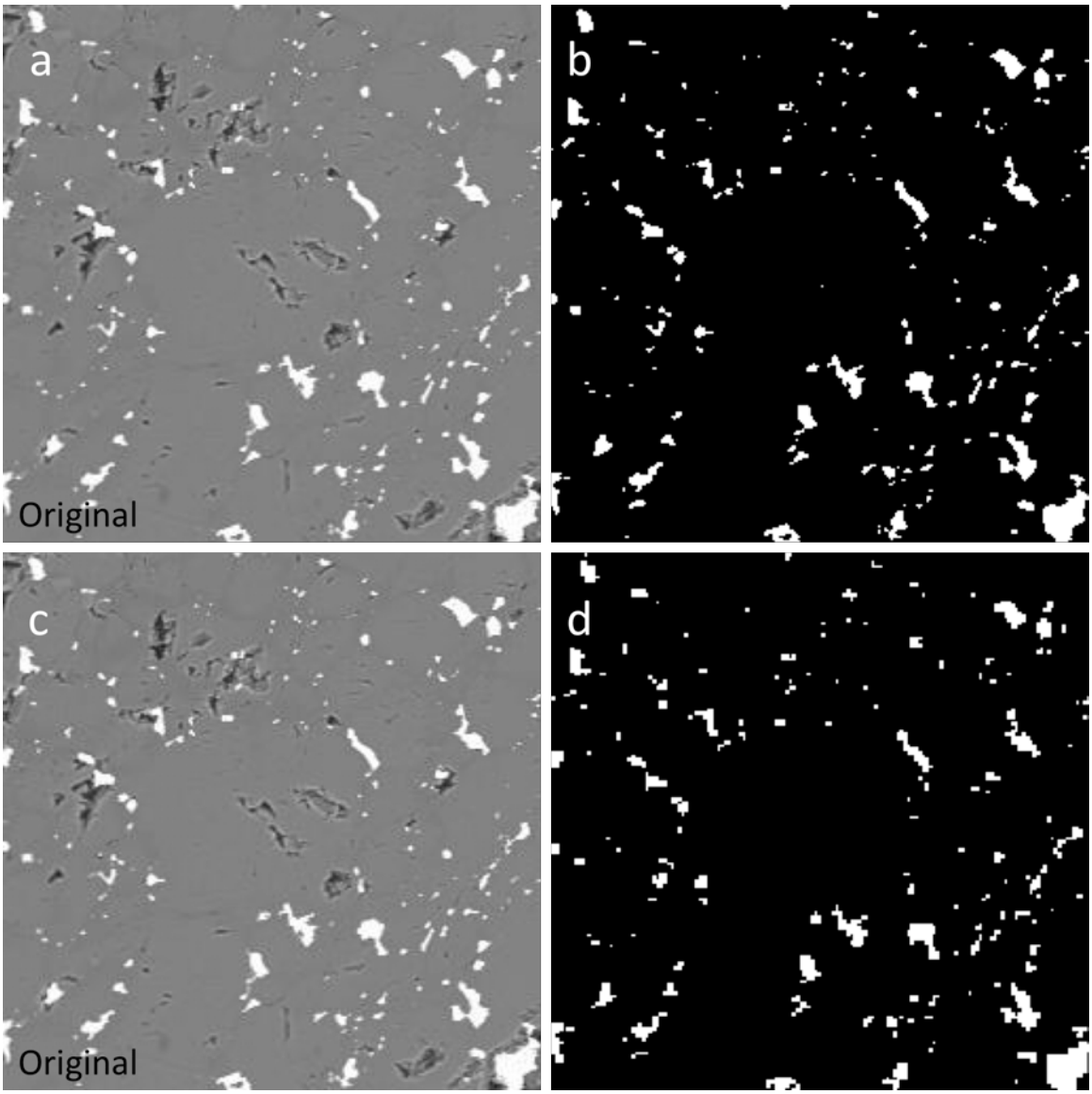

Figure 10